PHYSICAL REVIEW D **95,** 036020 (2017)

In-medium spectral functions of vector- and axial-vector mesons from the functional renormalization group

Christopher Jung,[1,2] Fabian Rennecke,[1,3] Ralf-Arno Tripolt,[4] Lorenz von Smekal,[1] and Jochen Wambach[2,4]

[1]*Institut für Theoretische Physik, Justus-Liebig-Universität Giessen, Heinrich-Buff-Ring 16, 35392 Giessen, Germany*

[2]*Theoriezentrum, Institut für Kernphysik, Technische Universität Darmstadt, Schlossgartenstrasse 2, 64289 Darmstadt, Germany*

[3]*Institut für Theoretische Physik, Ruprecht-Karls-Universität Heidelberg, Philosophenweg 16, 69120 Heidelberg, Germany*

[4]*European Centre for Theoretical Studies in Nuclear Physics and Related Areas (ECT*) and Fondazione Bruno Kessler, Villa Tambosi, Strade delle Tabarelle 286, I-38123 Villazzano (TN), Italy*

(Received 31 October 2016; published 23 February 2017)

In this work, we present the first results on vector- and axial-vector meson spectral functions as obtained by applying the nonperturbative functional renormalization group approach to an effective low-energy theory motivated by the gauged linear sigma model. By using a recently proposed analytic continuation method, we study the in-medium behavior of the spectral functions of the ρ and a_1 mesons in different regimes of the phase diagram. In particular, we demonstrate explicitly how these spectral functions degenerate at high temperatures as well as at large chemical potentials, as a consequence of the restoration of chiral symmetry. In addition, we also compute the momentum dependence of the ρ and a_1 spectral functions and discuss the various timelike and spacelike processes that can occur.

DOI: 10.1103/PhysRevD.95.036020

I. INTRODUCTION

A major challenge in quantum chromodynamics (QCD) is to explore the phase structure of strong-interaction matter, including possible phase transitions and the existence and location of a critical endpoint (CEP) [1,2]. In experiments one performs heavy-ion collisions to produce extremely high-energy densities leading to new phases such as the quark-gluon plasma (QGP). To get insights into the entire space-time history of the collision process, real photons and dileptons are particularly useful probes since they have negligible interactions with the hadronic fireball [3–5]. In this context the decay of vector mesons (located in the low invariant-mass regime), and here especially the ρ meson, is interesting since the quantum numbers of vector mesons allow them to directly decay into dileptons [6]. For this reason the in-medium properties of the ρ meson have received considerable attention [7–9]. By analyzing dilepton spectra at low invariant masses, one tries to find evidence for chiral symmetry restoration or the existence of a CEP [10,11].

The basis for calculating vector-meson spectral functions is a physically reasonable description of vector mesons within effective models for QCD. The first model including vector mesons was introduced by Sakurai in the 1960s [12] who generalized the known gauge principle from QED to local $SU(2)_V$ isospin symmetry present in QCD. This concept was in accordance with experimental observations and is referred to as the vector-meson dominance model (VMD) [13]. To study chiral symmetry and its breaking pattern in more detail, the gauge concept of Sakurai was extended to the chiral symmetry group $SU(2)_L \times SU(2)_R$ as a local gauge symmetry, where the a_1 meson as a chiral partner of the ρ meson also appears as a gauge boson [14], thus leading to the "gauged linear sigma model." Another possibility is to impose a global chiral symmetry rather than a local one [15–17].

The feasibility of calculating in-medium spectral functions from the functional renormalization group (FRG) [18–26] has been demonstrated in [27–29]. Apart from the absence of a fermion sign problem at finite chemical potential, one of the main advantages of the method proposed is that the analytic continuation from Euclidean to Minkowski space-time can be performed in a well-defined and simple way. Moreover, since thermal and quantum fluctuations are taken into account properly within the FRG approach, the method is also well suited to treat critical phenomena like phase transitions [30–37]. Aside from the nonperturbative method presented here, there are also intriguing phenomenological approaches to address the degeneracy of vector- and axial-vector spectral functions based on sum rules and loop expansions of gauged chiral Lagrangians [38,39].

In this paper we present first results for the ρ and a_1 meson spectral functions from the FRG based on the gauged linear sigma model, inspired by [16]. We derive flow equations for the real-time two-point functions of ρ and a_1 mesons which are obtained from their Euclidean counterparts via an analytic continuation on the level of the flow equations [27,40–42]. This allows access to real-time quantities such as pole masses and decay widths which we

calculate in various regions of the phase diagram predicted by the model, especially along the axis of vanishing chemical potential and the μ-axis across the CEP. Since our FRG treatment is thermodynamically consistent and symmetry preserving, the in-medium modifications of the spectral functions can be stringently connected to the restoration of chiral symmetry because the order parameter for chiral symmetry breaking and the spectral functions are obtained self-consistently.

The paper is organized as follows. We first motivate the model used and our ansatz for the quantum effective action in Sec. II A. We then discuss the salient features of the FRG as a nonperturbative method, as well as the resulting flow equations in Sec. II B. After going through some details concerning the numerical implementation in Sec. III A, we discuss the phase structure of the model as well as the T- and μ-dependent Euclidean and pole masses of the particles in Sec. III B. We then present ρ and a_1 spectral functions at finite temperature and chemical potential, first for vanishing external spatial momentum in Sec. III C and then for finite external spatial momentum in Sec. III D. We conclude by giving a summary in Sec. IV and present more details concerning the derivation of the flow equations, the analytic continuation procedure, the available processes and explicit expressions in Appendixes A–F.

II. THEORETICAL SETUP

A. Extended linear sigma model with quarks

In this section we present a simple low-energy model of two-flavor QCD that captures the main features relevant for the description of the ρ and a_1 mesons which is based on a previous work concerning the description of vector mesons in QCD [16]. In that work the connection of the effective action with QCD is given by successively integrating out quantum fluctuations starting from QCD at high energies. We focus on the dynamical generation of mesons but note that a similar reasoning can be applied to the formation of baryons.

The increasing strength of the strong coupling α_s with decreasing energy scale leads to strong two-quark-two-antiquark correlations. This naturally gives rise to effective quark-antiquark scattering channels $\lambda_i(\bar{\psi}T_i\psi)^2$ with the effective couplings $\lambda_i \propto \alpha_s^2$ and the tensor structures T_i. Hence, the QCD effective action naturally assumes the form of a gauged Nambu-Jona-Lasinio (NJL) model. With increasing α_s, the λ_i also increase until they eventually diverge. These divergences signal the formation of bound states and resonances in the quark-antiquark scattering channels. Since this applies, in particular, to the scalar-isoscalar channel, chiral symmetry breaking is dynamically generated.

We compute spectral functions from FRG flows which, in essence, are based on the fluctuations of off-shell degrees of freedom (see Sec. II B). Hence, the lightest particles give the most relevant contributions in the low-energy regime. For two quark flavors the dynamically most relevant mesons are pions as they are the pseudo-Goldstone bosons of spontaneous chiral symmetry breaking. Their chiral partner, the scalar σ meson, has to be included into our effective description as well. For two flavors, chiral $SU(2)_L \times SU(2)_R$ symmetry is locally isomorphic to $O(4)$ and we need both the isotriplet of pions, $\vec{\pi}$, and the isoscalar σ for the construction of chiral invariants. Furthermore, the σ mode is the critical mode at the CEP; i.e., it becomes exactly massless there. To capture chiral symmetry restoration in the spectral functions of the phenomenologically relevant ρ meson, we also include its chiral partner, the a_1 meson. The corresponding four-quark channels of the effective NJL-type action are given by

$$\mathcal{L}_{(4q)} = \frac{\lambda_S}{2}[(\bar{\psi}\psi)^2 - (\bar{\psi}\gamma_5\vec{\tau}\psi)^2] - \frac{\lambda_V}{2}[(\bar{\psi}\gamma_\mu\vec{\tau}\psi)^2 - (\bar{\psi}\gamma_\mu\gamma_5\vec{\tau}\psi)^2], \tag{1}$$

where $\vec{\tau}$ are the Pauli matrices. The first term of Eq. (1) has the quantum numbers of σ and π mesons, and the second term has those of ρ and a_1 mesons, respectively. The formation of mesons at the scale of chiral symmetry breaking will be reflected by poles in the corresponding quark-antiquark scattering channel. Their properties at low energies can, in principle, be studied by computing the full momentum dependence of λ_S and λ_V. We resort to a simpler treatment by explicitly introducing mesons, as they are the dominant low-energy degrees of freedom. This is done by partially bosonizing the four-quark interaction Eq. (1) by means of a Hubbard-Stratonovich transformation. This yields the following mixed fermionic-bosonic contribution to the effective action,

$$\mathcal{L}_{(\mathrm{FB})} = \frac{1}{2}m_S^2(\sigma^2 + \vec{\pi}^2) + h_S\bar{\psi}(\sigma + i\gamma_5\vec{\tau}\,\vec{\pi})\psi + \frac{1}{2}m_V^2[(\vec{\rho}^{\,\mu})^2 + (\vec{a}_1^{\,\mu})^2] + ih_V\bar{\psi}(\gamma_\mu\vec{\tau}\vec{\rho}^{\,\mu} + \gamma_\mu\gamma_5\vec{\tau}\vec{a}_1^{\,\mu})\psi, \tag{2}$$

which directly reflects the fermionic pairing through the scalar and vector Yukawa couplings h_S and h_V. In the present case, the scale of bosonization is chosen to be the UV cutoff Λ of our effective description. There, Eq. (1) is equivalent to Eq. (2) also on the quantum level if

$$\lambda_S = \frac{h_S^2}{m_S^2} \quad \text{and} \quad \lambda_V = \frac{h_V^2}{m_V^2}. \tag{3}$$

Note that chiral symmetry breaking, i.e., a diverging λ_S, is signaled by a sign change of the mass parameters m_S^2 in analogy to Ginzburg-Landau theory. In QCD the scale of meson formation emerges dynamically and is not

introduced by hand. To capture this transition within a unified framework, one can use dynamical hadronization as put forward for QCD in [43,44] and applied to vector mesons in the vacuum in [16]. Since we are only interested in the low-energy effective theory here, we postpone a treatment within full QCD to future work.

If we further integrate out fluctuations, the mesons which were formally introduced as auxiliary fields in Eq. (2) become dynamical, and higher-order effective meson interactions are generated. Furthermore, the gauge sector of QCD develops a mass gap and eventually decouples from the system at low energies. Here we assume that the gluons are fully integrated out at the UV cutoff Λ of the low-energy effective theory.

While, in principle, all meson interactions consistent with the global and local symmetries of the system are present in the mesonic part of the effective action, we restrict ourselves to the convenient case of a gauged linear sigma model [14]. To this end, we assume that the meson sector has a local chiral $SU(2)_L \times SU(2)_R$ symmetry. This assumption is particularly powerful since the interactions involving vector mesons are completely fixed by gauge symmetry. This reduces the potentially large number of effective couplings to one gauge coupling g. Putting all this together finally leads us to the following effective action:

$$\begin{aligned}\Gamma_k = \int d^4x [&\bar{\psi}(\partial - \mu\gamma_0 + h_S(\sigma + \mathrm{i}\vec{\tau}\vec{\pi}\gamma_5) \\ &+ \mathrm{i}h_V(\gamma_\mu \vec{\tau}\vec{\rho}^\mu + \gamma_\mu\gamma_5\vec{\tau}\vec{a}_1^\mu))\psi + U_k(\phi^2) - c\sigma + \frac{1}{2}(\partial_\mu\phi)^2 \\ &+ \frac{1}{8}\mathrm{Tr}(\partial_\mu V_\nu - \partial_\nu V_\mu)^2 - \mathrm{i}gV_\mu\phi\partial_\mu\phi \\ &- \frac{1}{2}g^2(V_\mu\phi)^2 + \frac{1}{4}m_{k,V}^2\mathrm{Tr}(V_\mu V_\mu)] + \Delta\Gamma_{\pi a_1}, \end{aligned} \tag{4}$$

where $U_k(\phi^2)$ is the $O(4)$ symmetric effective potential and a function of the chiral invariant ϕ^2 with $\phi = (\vec{\pi}, \sigma)^T$. This constitutes the lowest order in a gradient expansion of the effective action and implies, in particular, that wave-function renormalizations are not taken into account. The source term $-c\sigma$ stems from the bosonization of the current-quark mass term of the QCD action. It therefore accounts for the explicit chiral symmetry breaking through explicit quark masses. Hence, the pions are pseudo-Goldstone bosons with finite mass, and the chiral phase transition is a crossover at small chemical potentials.

The vector mesons are given in the adjoint representation of $O(4)$ with

$$V_\mu = \vec{\rho}^\mu\vec{T} + \vec{a}_1^\mu\vec{T}^5. \tag{5}$$

We define the $\mathfrak{so}(4)$ matrices,

$$(T_i)_{jk} = \begin{pmatrix} -i\epsilon_{ijk} & \vec{0} \\ \vec{0}^T & 0 \end{pmatrix}, \qquad (T_i^5) = \begin{pmatrix} 0_{3\times3} & -i\vec{e}_i \\ i\vec{e}_i^T & 0 \end{pmatrix}, \tag{6}$$

with $i, j, k \in \{1, 2, 3\}$ and $\vec{e}_i^T = (\delta_{1i}, \delta_{2i}, \delta_{3i})$. They obey the following commutation relations:

$$[T_i, T_j] = i\epsilon_{ijk}T_k, \quad [T_i^5, T_j^5] = i\epsilon_{ijk}T_k, \quad [T_i, T_j^5] = i\epsilon_{ijk}T_k^5, \tag{7}$$

and therefore $T_i^L = \frac{1}{2}(T_i - T_i^5)$ and $T_i^R = \frac{1}{2}(T_i + T_i^5)$ form representations of $SU(2)_L$ and $SU(2)_R$. The mesons transform under these flavor rotations as

$$\phi \to U\phi, \qquad V_\mu \to UV_\mu U^\dagger, \tag{8}$$

with $U = e^{i\vec{\alpha}\vec{T} + i\vec{\beta}\vec{T}^5}$ and parameters $\vec{\alpha}$ and $\vec{\beta}$.

As already mentioned, we construct the vector-meson part of the effective action by gauging chiral symmetry. The vector field V_μ then naturally arises as a gauge field. Its interactions with the scalar and pseudoscalar mesons result from minimal coupling $(D_\mu\phi)^2/2$ with the covariant derivative $D_\mu = \partial_\mu - igV_\mu$. The kinetic term of the vector mesons as well as their self-interactions arise from the field-strength term $\mathrm{tr}V_{\mu\nu}V_{\mu\nu}/8$ with the field-strength tensor $V_{\mu\nu} = i[D_\mu, D_\nu]/g$. Since the dominant contributions to the vector-meson spectral functions stem from the decay channels that involve scalar and pseudoscalar mesons, we have neglected the vector-meson self-interactions here. Furthermore, it has been shown in [16] that the vector mesons are always decoupled from the dynamics of the system in Euclidean space-time. Our computation of the spectral functions uses the solution of the Euclidean system as input, and therefore vector-meson self-interactions do not play a role for this input. However, they are important for a quantitative description of vector-meson spectral functions. As the focus of the present work is on the qualitative connection between chiral symmetry restoration and vector-meson spectral functions, we postpone a more realistic description to future work.

A soft breaking of the chiral gauge symmetry is induced by the explicit vector-meson mass term in Eq. (4). However, the Yukawa interaction terms also explicitly break this symmetry. Hence, Γ_k only possesses global chiral symmetry and, as opposed to a pure gauged linear sigma model, the ρ meson does not couple to a conserved local current. An immediate consequence is that the vector-meson self-energies are not purely transversal.

Lastly, we discuss the term $\Delta\Gamma_{\pi a_1}$ in Eq. (4). If the mesons acquire a nonvanishing vacuum expectation value $\phi_0 = (\sigma_0, \vec{0})$ due to spontaneous chiral symmetry breaking, a contribution of the form

$$-\int_x g\sigma_0 \vec{a}_1^{\mu} \cdot \partial_\mu \vec{\pi} \subset \Gamma_k \tag{9}$$

yields an off-diagonal meson propagator. This is referred to as $\pi - a_1$ mixing. We eliminate this mixing, i.e., diagonalize the meson propagator, by a redefinition of the a_1 field:

$$\vec{a}_1^{\mu} \to \vec{a}_1^{\mu} + \frac{g\sigma_0}{m_{k,V}^2 + g^2\sigma_0^2} \partial_\mu \vec{\pi}. \tag{10}$$

If we insert this replacement into Γ_k, various new terms are generated, which we subsume in $\Delta\Gamma_{\pi a_1}$. Among the numerous new terms in the effective action, only three are potentially relevant in the present work. This is rooted in the approximations we employ here. First of all, we only take the fluctuations of scalar and pseudoscalar mesons and quarks into account. Hence, all vertices that would lead to vector mesons in the loops can be ignored. Furthermore, our construction of the effective action is based on a low-momentum expansion; i.e., we use the lowest-order derivative expansion, and hence only contributions up to second order in the derivatives have to be retained. Lastly, the scalar and pseudoscalar meson self-interactions are defined from the effective potential $U_k(\phi^2)$ and are therefore momentum independent by construction. Thus, every modification of the corresponding vertices that involves space-time derivatives can also be ignored. The remaining terms yield

$$\Delta\Gamma_{\pi a_1} = \int_x \left\{ g\sigma_0 \vec{a}_1^{\mu} \cdot \partial_\mu \vec{\pi} - \frac{1}{2} \frac{g^2\sigma_0^2}{m_{k,V}^2 + g^2\sigma_0^2} (\partial_\mu \vec{\pi})^2 - \frac{g^2\sigma_0^2}{m_{k,V}^2 + g^2\sigma_0^2} \vec{\rho}^{\mu} \times \vec{\pi} \cdot \partial_\mu \vec{\pi} \right\}. \tag{11}$$

The first term in the first line of this equation cancels the mixing term Eq. (9) and thus leads to a diagonal meson propagator in the broken phase. The second term generates a nontrivial wave-function renormalization for the pions. The effects of wave-function renormalizations are not the subject of the present analysis and are therefore postponed to future work. Hence, we drop this contribution. The term in the second line of Eq. (11) modifies the $\pi\pi\rho$ vertex $\Gamma^{(3)}_{k,\pi\pi\rho}$. This has to be taken into account when we compute loop diagrams, e.g., for the two-point function of the pion. The corresponding modified Feynman rule for this vertex can be found in Eq. (A20). We note that the redefinition of the a_1 field in Eq. (10) involves running couplings. Thus, strictly speaking, the new a_1 field is explicitly renormalization-group scale dependent. A self-consistent way to treat this scale-dependent field has been put forward in [16]. However, this only gives minor quantitative corrections. Since our focus is on qualitative effects, we can readily ignore this here.

In the described model we have no mechanism included which describes the phenomenon of confinement. The Polyakov loop within the Polyakov-quark-meson model, usually used to describe confinement in terms of thermodynamics [32,45–47], is not able to suppress unphysical quark-antiquark decays in the confined phase, cf. Appendix D. A physically reasonable way to include confinement in such low-energy models is also left to future work.

B. Functional renormalization group and flow equations

The FRG provides a powerful, nonperturbative tool to investigate the transition from microscopic to macroscopic scales and is widely used in statistical physics and quantum field theory. The central object in this framework is the so-called effective average action Γ_k. It interpolates between the microscopic action $\Gamma_{k=\Lambda}$ at some chosen UV cutoff Λ and the full quantum effective action $\Gamma = \Gamma_{k\to 0}$ where all quantum fluctuations are included and macroscopic properties of the system can be extracted. The scale-dependent effective average action Γ_k only includes fluctuations with momenta larger than the RG scale k which, on a technical level, is achieved by introducing a regulator function R_k. Starting at $k = \Lambda$ one then successively lowers k until arriving at the full quantum effective action Γ in the infrared. The change of the effective average action Γ_k with the RG scale k is thereby governed by the Wetterich equation [48]

$$\partial_k \Gamma_k = \frac{1}{2} \mathrm{Tr}[\partial_k R_k^{\phi} (\Gamma_k^{(2)}[\phi] + R_k^{\phi})^{-1}]. \tag{12}$$

Here we apply this concept to the low-energy model introduced in Sec. II A (see Fig. 1 for a diagrammatic representation of the resulting flow equation). The Wetterich equation then turns into a flow equation for the effective mesonic potential U_k [see also Eq. (A1) for its explicit form]. We note that for isospin symmetric matter with an equal number of up and down quarks, the isovector ρ and a_1 mesons do not contribute to the effective potential.

Flow equations for n-point functions are, in general, obtained by taking n functional derivatives of the Wetterich equation with respect to certain fields. The flow equations then naturally contain up to $n+2$-point functions, which

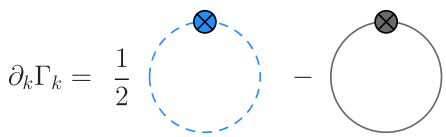

FIG. 1. Flow equation for the effective action of the model defined by Eq. (4) in diagrammatic form. The dashed blue line is associated with propagators of the σ and π mesons, the solid black line is associated with the quark propagator, and the crossed circles represent the regulator insertions $\partial_k R_k$.

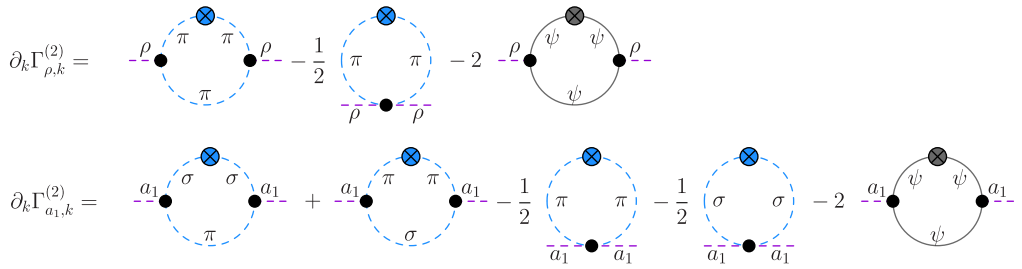

FIG. 2. Flow equations for the ρ and a_1 two-point functions in diagrammatic form. Vertices are indicated by black filled dots, regulator insertions by crossed circles. The color of the lines and regulators represents the type of field: blue for scalar and pseudoscalar mesons, black for fermions, and purple for vector mesons.

leads to an infinite set of coupled equations. In order to solve this system, one has to introduce truncations. In the present work we extract three- and four-point functions appearing on the rhs of the flow equations from the ansatz of the effective average action, Eq. (4), as done, for example, in [27,28]. An improved truncation taking into account full momentum-dependent vertices and solving the flow equations for two-point functions iteratively is left to future studies.

Following this strategy, we obtain flow equations for the ρ and a_1 two-point functions as a closed system of equations

$$\partial_k \Gamma^{(2)}_{k,\rho}(p) = J^{\pi\pi}_{k,\rho}(p) - \frac{1}{2} I^{\pi}_{k,\rho} - 2J^{\psi\bar{\psi}}_{k,\rho}(p), \tag{13}$$

$$\partial_k \Gamma^{(2)}_{k,a_1}(p) = J^{\sigma\pi}_{k,a_1}(p) + J^{\pi\sigma}_{k,a_1}(p) - \frac{1}{2} I^{\pi}_{k,a_1} - \frac{1}{2} I^{\sigma}_{k,a_1} - 2J^{\psi\bar{\psi}}_{k,a_1}(p), \tag{14}$$

where momentum-dependent and momentum-independent loop functions appear (see Appendixes A and F for the projected flow equations and explicit expressions, including the vertices). The diagrammatic form of these equations is illustrated in Fig. 2.

The flow equations are then solved by starting with the microscopic theory at a UV cutoff and then integrating out momentum shells down to the scale k. The effective average action Γ_k as well as the mesonic two-point functions $\Gamma^{(2)}_k$ then incorporate fluctuations with momenta larger than the RG scale k. For technical details we refer to Sec. III A and Appendix A.

III. RESULTS AND DISCUSSION

A. Numerical implementation

In order to solve the flow equations for the retarded two-point functions of the ρ and a_1 mesons, we first solve the flow equation for the effective potential U_k, cf. Appendix A. This is done by discretizing the effective potential in σ-field direction, which yields a set of coupled ordinary differential equations that can then be solved with common methods. The parameters for the effective potential at the UV scale $\Lambda = 1500$ MeV,

$$U_\Lambda = b_1\phi^2 + b_2\phi^4, \tag{15}$$

the explicit symmetry-breaking constant c, as well as the scalar and vector Yukawa couplings are given in Table I. They are chosen such that in the vacuum we have, with a constituent quark mass of $m_\psi = 300$ MeV at the IR scale $k_{\mathrm{IR}} = 40$ MeV, phenomenologically reasonable values for the masses of the pion and σ meson [corresponding to the $f_0(500)$ resonance] and the pion decay constant (here identified with the global minimum of the σ field at σ_0): $m_\pi = 140$ MeV, $m_\sigma = 557$ MeV, $f_\pi \equiv \sigma_0 = 93.0$ MeV.

Note that the meson masses here are Euclidean curvature masses, i.e., the mass parameters that determine the curvatures of the mesonic effective potential which agree with the zero-momentum limits of the corresponding Euclidean mesonic two-point functions. They can differ from the physical masses which are the so-called pole masses, i.e., the zeros of the analytically continued two-point functions at timelike momenta. Apart from potential wave-function renormalization factors, beyond the leading-order derivative expansion employed here, the differences will be small for the pion, for example, because its zero-momentum correlator is of course dominated by the well-isolated pion pole. For heavier and not so well-isolated bound states and resonances such as the ρ and a_1 mesons, these differences will be important, however.

The Euclidean curvature mass of the ρ meson is given by the vector-meson mass parameter, i.e., the quadratic coupling $m^2_{k,V}$ in the effective action in Eq. (4), cf. Appendix A. By using the RG flow of the effective potential and its derivatives as input, the flow equation for $m^2_{k,V}$, Eq. (A27), can be solved. The initial condition for $m^2_{\Lambda,V}$ at the UV scale

TABLE I. Parameter set used in this work.

b_1[MeV^2]	b_2	c[MeV^3]	$h_S = h_V$	g	$m_{\Lambda,V}$ [MeV]
857300	0.2	1.8228×10^6	3.226	11.4	1450

$\Lambda = 1500$ MeV, as well as the scale-independent gauge coupling g as chosen in Table I, then results in the vacuum pole masses m_ρ^p and $m_{a_1}^p$: $m_\rho^p = 789.3$ MeV and $m_{a_1}^p = 1274.7$ MeV. They thus reproduce the physical masses of ρ and a_1 reasonably well. Since fine-tuning the UV parameters to adjust these pole masses to the physical ones more precisely is a rather tedious task, we are content with this level of agreement for our qualitative study here. We also note that we use the zero crossing of the real part of the retarded two-point function, cf. Appendix D, as an estimate of the real part of the complex pole of the corresponding propagator on the unphysical Riemann sheet in the complex energy plane for a resonance. This is justified, as long as the width of the resonance, i.e., the imaginary part of $\Gamma^{(2,R)}$, is reasonably small. A more precise determination of the pole masses is possible by studying the analytic structure of $\Gamma^{(2,R)}$ or the spectral function on the second Riemann sheet of the complex energy plane. A promising method to perform such a study was recently proposed in [49] and will be used to obtain in-medium pole masses for broad resonances more accurately in the future.

For comparison, the corresponding Euclidean curvature masses with the same UV parameters result as $m_\rho = 1298.3$ MeV and $m_{a_1} = 1676.3$ MeV. Parts of the discrepancy between curvature and pole masses should be compensated by the inclusion of wave-function renormalization factors, i.e., by going to higher orders in the gradient expansion. We reiterate, however, that there is no *a priori* reason for the two to agree. In particular, the Euclidean curvature masses do not have a direct physical meaning and should rather be seen as parameters that determine the physical pole masses.

In a last step the flow equations for the real and the imaginary parts of the retarded two-point functions are solved at the grid point of the IR minimum σ_0, from which the spectral functions can be obtained as described in Appendix B.

B. Phase structure and curvature masses

In this section we briefly discuss the flow of the Euclidean curvature masses as well as the phase structure and the T and μ dependence of the quark and meson masses which serve as an important input for the computation of the spectral functions.

The RG flow of the scale-dependent Euclidean curvature masses defined in Appendix A is shown in Fig. 3. Starting the flow in the chirally restored phase at the UV cutoff scale $\Lambda = 1500$ MeV, the masses of the chiral partners start out to be degenerate as well. Successively lowering the RG scale k, both the ρ and the a_1 meson masses slightly drop together at first. Eventually, however, the fermionic fluctuations drive the minimum of the k-dependent bosonic effective potential away from zero and into the chirally broken phase with a nonvanishing order parameter σ_0, which hence also leads to a mass splitting of the chiral

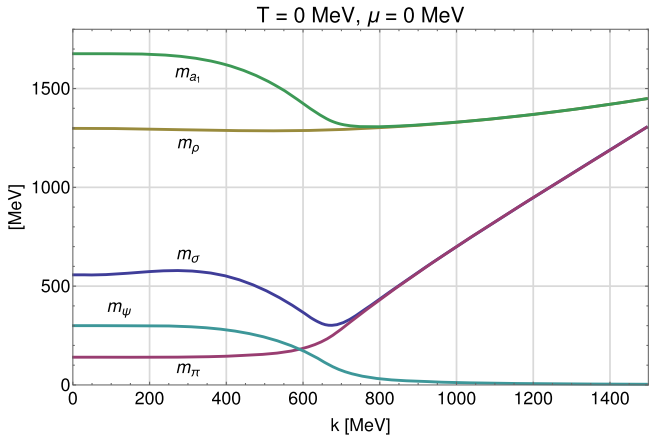

FIG. 3. Flow of the scale-dependent Euclidean curvature masses of mesons and the constituent quark mass with the RG scale k at $T = 0$ MeV and $\mu = 0$ MeV.

partners. As seen in Fig. 3, this occurs at a scale of around $k_{\chi\mathrm{SB}} \approx 700$ MeV. Below that scale, the mass of the a_1 meson begins to rise, whereas the ρ meson mass remains approximately constant during the complete flow. We notice that the vector-meson masses are always larger than the scale k and are hence always decoupled from the flow, which also has been observed in [16]. The dynamics in Euclidean space-time are therefore completely determined by the pion and the σ meson as well as the quarks. The overall behavior with the RG scale k qualitatively resembles the temperature dependence of quark and meson masses at $\mu = 0$ MeV in Fig. 4.

Our findings for the behavior of the ρ and a_1 masses in the hadronic phase are in agreement with the results in [16]. This implies that the masses are insensitive to gluon fluctuations in this regime. However, in the vicinity and above the chiral symmetry breaking scale, $k_{\chi\mathrm{SB}}$, gluon fluctuations induce a rapid increase of the meson masses and thus guarantee that they vanish from the physical

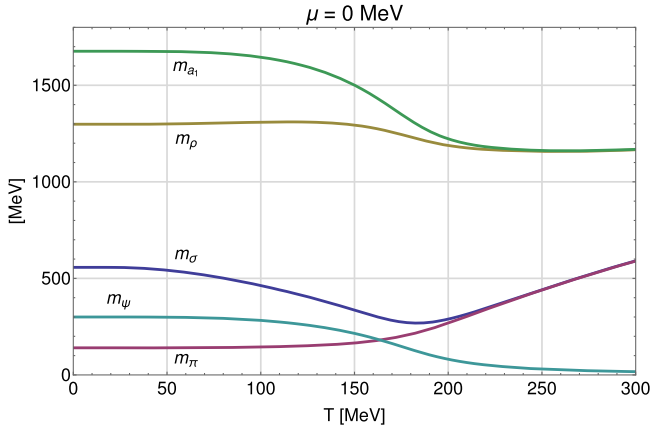

FIG. 4. Euclidean curvature masses of mesons and constituent quark mass at the IR scale vs temperature at $\mu = 0$ MeV.

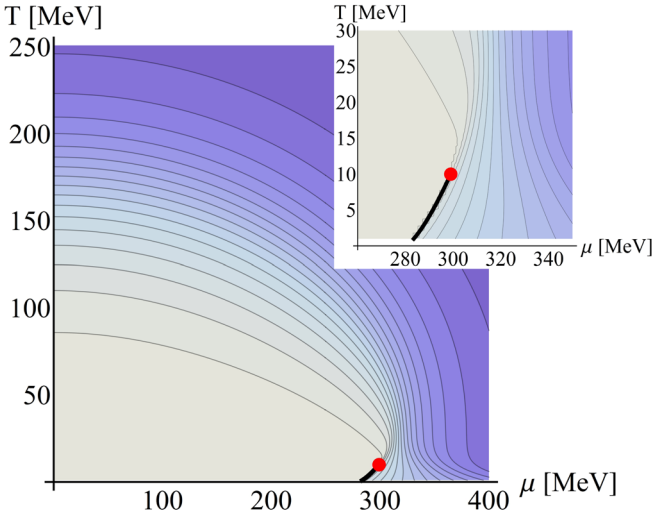

FIG. 5. Phase diagram of the quark-meson model as a contour plot of the order parameter for chiral symmetry $\sigma_0(T,\mu)$. The value of $\sigma_0(T,\mu)$ decreases with increasing temperature and chemical potential as indicated with a darker color. The CEP is indicated as a red dot, whereas the first-order phase boundary is indicated by a black line.

spectrum in the quark-gluon regime. While we also observe this behavior here, it is much more pronounced in [16], where gluon fluctuations were explicitly included. As a consequence, the scaling of the a_1 mass in the vicinity of $k_{\chi\mathrm{SB}}$ is qualitatively different.

The phase diagram of the model we use, which is a quark-meson model on the level of the effective potential, is depicted in Fig. 5 (see also [27,30] for earlier studies on the quark-meson model). It is obtained by the location of the global minimum of the effective potential at the IR scale $\sigma_0 \equiv \sigma_0(T,\mu)$. With the parameters given in Table I we find a critical endpoint at around $(\mu_{\mathrm{CEP}}, T_{\mathrm{CEP}}) \approx (298, 10)$ MeV, which divides a crossover region from a first-order phase transition at lower temperatures. We note that the slope $dT/d\mu$ of the first-order line is very different from the one observed in mean-field studies (see e.g. [50]). In fact, the regime to the right of the first-order line, i.e., at large chemical potentials and low temperatures, is likely to be dominated by an inhomogeneous ground state which leads to unphysical effects like a negative entropy density in the present truncation. We therefore avoid this regime in the following and refer to [51] for further details.

The same Euclidean curvature masses of the mesons, plotted together with the constituent quark mass over temperature at $\mu = 0$ MeV in Fig. 4, are shown along the μ-axis at a constant temperature of $T = 10$ MeV across the CEP in Fig. 6. They behave as expected in a model based on chiral symmetry. For vanishing chemical potential, the Euclidean curvature masses of the chiral partners m_σ, m_π and m_ρ, m_{a_1} become degenerate at high temperatures, $T \gtrsim 200$ MeV. The quark mass m_ψ decreases, indicating the gradual restoration of chiral symmetry. For

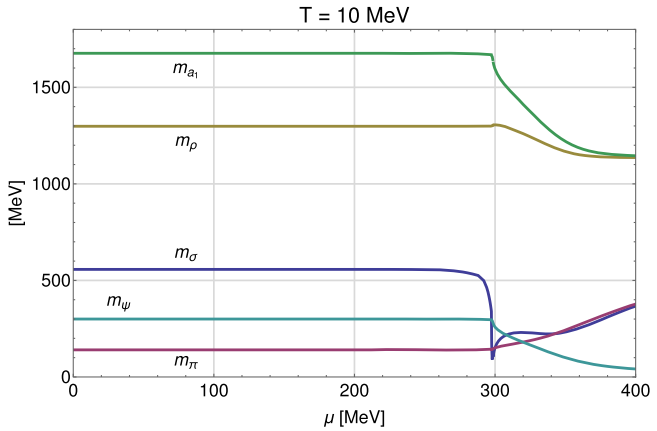

FIG. 6. Euclidean curvature masses of mesons and constituent quark mass vs chemical potential at $T = 10$ MeV.

a fixed temperature of $T = 10$ MeV the masses do not really change over a wide range of chemical potential, as expected from the Silver Blaze property [52]. Near the CEP at around $\mu_{\mathrm{CEP}} \approx 298$ MeV, the sigma mass drops significantly as expected at this second-order phase transition. In addition, the chiral condensate as well as the vector-meson masses decrease when crossing the CEP. For very high chemical potentials the masses of the chiral partners coincide again and the quark mass decreases, similar to the case of high temperature and vanishing chemical potential.

C. In-medium spectral functions at $|\vec{p}| = 0$

Before turning to the ρ and a_1 spectral functions at finite temperature and chemical potential, in this subsection for vanishing external spatial momentum, $|\vec{p}| = 0$, we will discuss the temperature dependence of the physically relevant vector-meson pole masses. They are obtained from the zero crossing of the real part of the two-point functions and are shown in Fig. 7 vs T at $\mu = 0$.

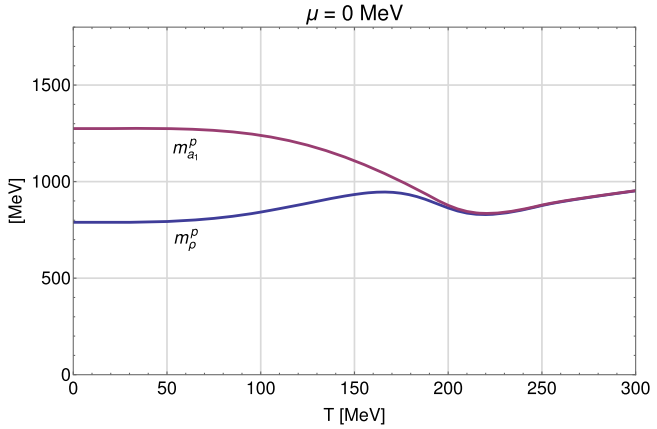

FIG. 7. Pole masses of ρ and a_1 mesons vs temperature at $\mu = 0$ MeV.

At $T = 0$ chiral symmetry is broken and the pole masses assume the vacuum values of $m_\rho^p = 789.3$ MeV and $m_{a_1}^p = 1274.7$ MeV for the UV parameters of Table I. With increasing temperature the difference between the pole masses decreases until they become degenerate at $T \approx 200$ MeV, i.e., at about the same temperature as the Euclidean curvature masses. The observed behavior supports the "melting-ρ scenario," where the ρ meson mass remains almost stable and the a_1 mass shifts towards the mass of the ρ meson [11,39].

In order to exhibit the T- and μ-induced modifications more clearly, Fig. 8 shows logarithmic plots of the ρ and a_1 spectral functions for vanishing chemical potential (left column) and for a fixed temperature of $T = 10$ MeV along the μ-axis towards the CEP (right column). At $T = 0$ MeV, the $\rho^* \to \pi + \pi$ threshold gives rise to a nonvanishing value of the ρ spectral function for $\omega \gtrsim 280$ MeV. For $\omega \gtrsim 600$ MeV the decay into quark-antiquark pairs becomes energetically possible and gives rise to another threshold in the spectral function. The spectral function of the a_1 meson exhibits the first threshold at $\omega \approx 600$ MeV, when the quark-antiquark decay becomes possible and the width then increases due to the mesonic decay channel $a_1^* \to \pi + \sigma$. In both spectral functions, the quark-antiquark decay strongly suppresses the pole mass peaks (see also Appendix D).

At finite temperature the a_1 meson can capture a pion from the heat bath to form a sigma meson, $a_1^* + \pi \to \sigma$. This capture process can occur when $\omega = E_{k,\sigma} - E_{k,\pi}$, i.e., for the difference of the effective quasiparticle energies of σ and π at the momentum scale k, cf. Appendix A. It is therefore bounded by $\omega \leq m_\sigma - m_\pi$. When the slopes of the quasiparticle branches of σ and π in the scale k get very close to one another during the FRG flow, i.e., when their difference $E_{k,\sigma} - E_{k,\pi}$ flows through a saddle point, or an approximate one, the spectral density develops a peak analogous to a van Hove singularity in the density of states in the electronic band structure of solids. Such a van Hove peak is seen in the a_1 spectral function in the left column of Fig. 8 for $T = 100$ MeV and 150 MeV, i.e., in the crossover region, just below the threshold of the capture process at $\omega = m_\sigma - m_\pi$. As the difference between the sigma and the pion mass tends to zero, this threshold moves to smaller and smaller energies when the temperature is further increased.

For temperatures around the crossover, the quark mass drops significantly as well, leading to a shift of the associated threshold to lower energies and a further broadening of the peaks in the spectral functions. For very high temperatures pole and curvature masses of the chiral partners degenerate, and the contribution from the capture process disappears. The former behavior is due to the direct link between the mass difference of ρ and a_1 with the chiral condensate [see Eq. (A3)]. The capture process disappears for the same reason, namely, because the π and σ masses also degenerate upon the melting of the condensate. Hence, the contributions of the dominant mesonic decay processes $\rho^* \to \pi + \pi$ and $a_1^* \to \pi + \sigma$ to the respective spectral functions degenerate as chiral symmetry gets restored as well. The same holds for the π and σ tadpole contributions shown in Fig. 2. Furthermore, the quarks become the lightest degrees of freedom and thus give the dominant contribution to the spectral functions in both channels. All these effects together result in the complete degeneration of the spectral functions of ρ and a_1 and provide a direct connection to chiral symmetry restoration.

Turning now to the dependence on the chemical potential in the right column of Fig. 8, at a temperature of $T = 10$ MeV, we observe that both spectral functions remain essentially unchanged from $\mu = 0$ up to values close to the critical endpoint, reflecting the Silver Blaze property as already mentioned in Sec. III B. Near the CEP, especially the a_1 spectral function shows sensitive modifications which are mainly induced by the dropping sigma mass. The main effect is that the threshold for the process $a_1^* \to \pi + \sigma$ moves to smaller energies with another van Hove peak from an approximate saddle point forming in $E_{k,\pi} + E_{k,\sigma}$ just above threshold. When hitting the CEP exactly, which is difficult in a numerical calculation especially when the mass of the σ meson drops so suddenly close to the endpoint as in Fig. 6, this threshold should be located exactly at the pion mass since the sigma mass vanishes completely there. The ρ spectral function, on the other hand, shows only small modifications. For very high chemical potentials and low temperatures we again see a degeneracy of the ρ and a_1 spectral functions. We note that $T = 50$ MeV and $\mu = 600$ MeV were chosen for the last plot in Fig. 8 in order to avoid the potentially problematic regime at low temperatures and large chemical potentials (see the discussion in Sec. III B).

D. Momentum dependence of spectral functions

As an instructive example for their momentum dependence, we show the transverse ρ and a_1 spectral functions at a temperature of $T = 100$ MeV and $\mu = 0$ MeV as a function of energy and momentum in Fig. 9 (see also Appendix A).

In the case of the ρ meson the timelike and spacelike regimes are clearly separated. While the decay thresholds of the $\rho^* \to \pi + \pi$ and the $\rho^* \to \bar{\psi} + \psi$ process are Lorentz-boosted to higher energies as the spatial momentum increases, the spacelike regime, where $\omega < |\vec{p}|$, is homogeneously filled up by the spacelike processes, cf. Eq. (E7). We note that in the vacuum the spectral function would be zero in the spacelike regime.

A similar behavior is observed for the a_1 spectral function. The thresholds associated with the timelike processes are correctly boosted to higher energies, while the spacelike regime does not show any particular structure for the a_1 either. In contrast to the ρ spectral function, however, there is no clear separation between the timelike and spacelike regimes since the process $a_1^* + \pi \to \sigma$

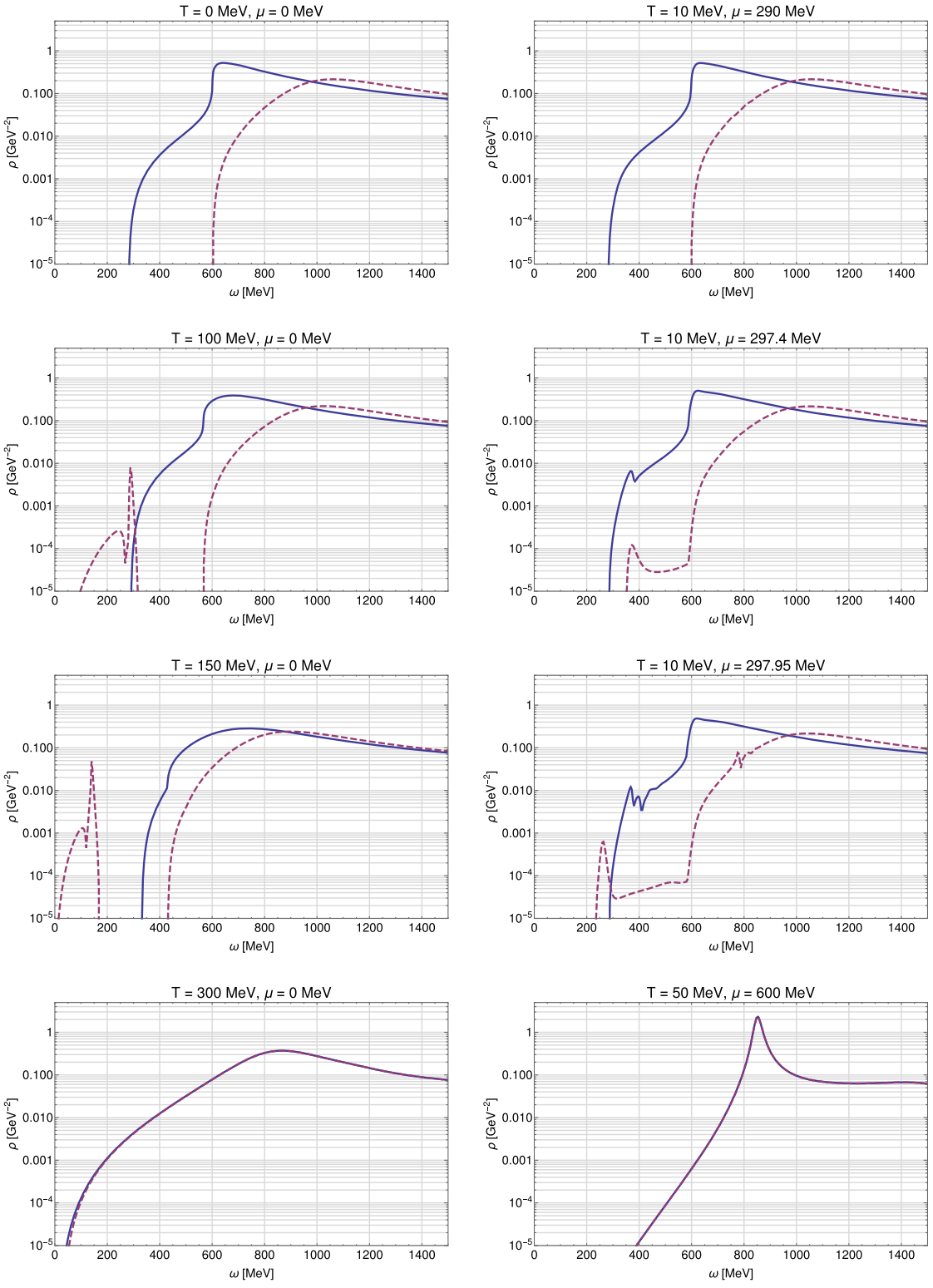

FIG. 8. Spectral functions of ρ (solid blue) and a_1 (dashed purple) meson vs external energy ω at $|\vec{p}| = 0$ shown for increasing temperature at $\mu = 0$ MeV (left column) and for increasing chemical potential at $T = 10$ MeV, towards the CEP (right column). For the last plot on the right-hand side we chose $T = 50$ MeV and $\mu = 600$ MeV in order to avoid a thermodynamically problematic regime in the phase diagram (see Sec. III B for details).

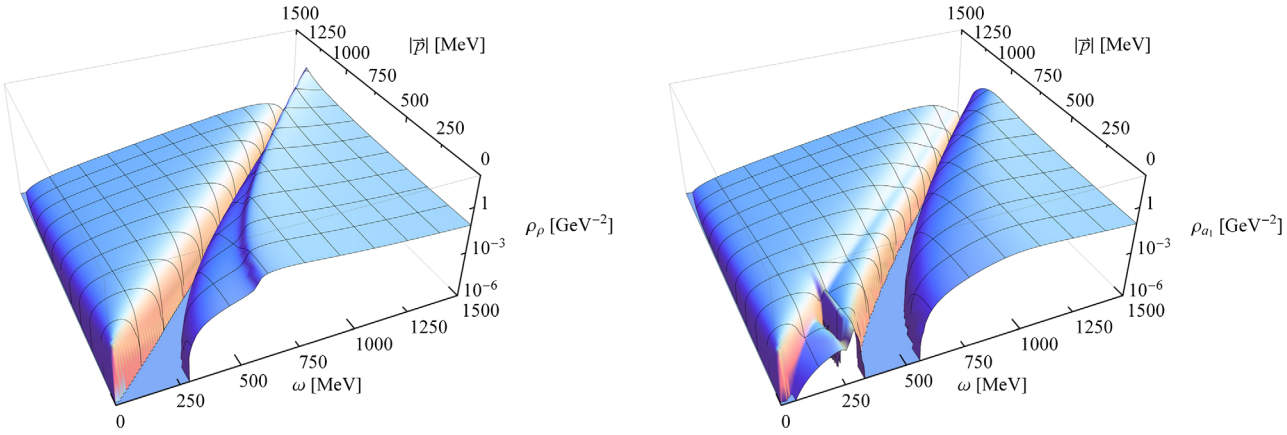

FIG. 9. The transverse ρ (left) and a_1 (right) spectral functions, $\rho_\rho(\omega, \vec{p})$ and $\rho_{a_1}(\omega, \vec{p})$, are shown versus external energy ω and external spatial momentum $\vec{p}$ at $T = 100$ MeV and $\mu = 0$ MeV. The timelike regime, $\omega > |\vec{p}|$, is Lorentz-boosted to higher energies as the momentum increases, while the spacelike regime, $\omega < |\vec{p}|$, is homogeneously filled up by the spacelike processes.

continuously connects both regions (see also [28]). We also note that, unlike the threshold for this capture process, the position of the van Hove peak in the a_1 spectral function, which occurs close to this threshold at $\omega = m_\sigma - m_\pi \approx 300$ MeV for $|\vec{p}| = 0$, remains essentially unaffected at finite momentum. Rather, this van Hove peak eventually merges with the structureless spacelike region.

We conclude this section by noting that the momentum-dependent spectral functions are closely connected to the real-time propagators and thus also allow access to static properties of the medium, such as transport coefficients in the appropriate limits [29].

IV. SUMMARY

Within an effective description for low-energy QCD, we have computed the in-medium spectral functions of the ρ and a_1 mesons using the FRG method. This allows for a simultaneous description of the chiral phase structure of QCD and the behavior of the mesonic spectral functions at finite temperature and density within a unified framework. The main question we have addressed here was how the in-medium modifications of the spectral functions of the chiral partners ρ and a_1 are connected to chiral symmetry restoration.

To illustrate this, we have used an effective low-energy model for two-flavor QCD based on a gauged linear sigma model augmented by dynamical constituent quarks. This construction was guided by requiring that both the dominant mesonic processes and the phase structure of QCD are treated on the same footing. Hence, in addition to the chiral partners, ρ and a_1, we have included the lightest pseudoscalar and scalar mesons π and σ [the latter being identified with the $f_0(500)$ resonance]. The momentum-independent self-interactions of the scalar and pseudoscalar mesons have been fully implemented by computing their effective potential. The leading-order interactions between the scalar and the vector sector have been included by invoking a gauge principle as in the gauged linear sigma model. The quark-meson interactions were constructed from QCD-inspired arguments concerning the dynamical generation of mesons from RG evolved quark-antiquark interactions in QCD. As we have demonstrated, this model allows for the simultaneous description of the chiral phase diagram in the $(T - \mu)$ plane and in-medium vector-meson spectral functions.

We have shown that by crossing the chiral phase boundary both at large temperature and large chemical potential, the spectral functions of the ρ and a_1 channels degenerate. The underlying mechanism which drives this degeneration becomes particularly lucid in the present approach. The mass splittings of the chiral partners decrease with the melting of the chiral condensate. As a result, the decay processes that determine the ρ and a_1 spectral functions degenerate, which finally leads to degenerate spectral functions. Furthermore, the decreasing constituent quark mass towards chiral symmetry restoration triggers the melting of the resonance peaks in the spectral functions. We have demonstrated this behavior along the temperature and chemical potential directions of the phase diagram. As it turns out, the ρ meson mass stays essentially constant, while the a_1 shows a significant mass shift towards the ρ when chiral symmetry restoration is approached. Chiral symmetry restoration is signaled by the degeneration of the spectral functions accompanied by a melting of the resonances rather than, e.g., a dropping of the mass as suggested by Brown and Rho [7]. Hence, our findings are in favor of the "melting scenario" concerning the interpretation of experimental dilepton data. This is in line with the results from phenomenological models [53] as well as results on the scaling of the vector-meson masses in QCD [16].

While our model captures the main qualitative features of the vector-meson spectral functions, there are various

directions left to be explored in future studies in order to arrive at a complete physical picture of the signatures of chiral symmetry restoration in vector-meson spectral functions. The most obvious shortcoming of our model is the lack of confinement. We show in Appendix D that, while the qualitative features of the spectral functions remain the same, the decay into on-shell quarks gives large contributions to the spectral functions deep in the hadronic phase where confinement should prevent such processes. In the present context, confinement manifests itself in positivity violation of the quark spectral functions (see e.g. [54]), and this should be accounted for in a more realistic description of chiral symmetry restoration. The incorporation of gluon fluctuations, which will certainly become relevant in the vicinity of the phase transition and at large frequencies/momenta, is also a crucial step in this direction and may be incorporated along the lines of [16]. This would also make the necessity of model parameter tuning obsolete. In order to capture the full momentum dependence of the propagators, we need to go beyond the classical momentum dependence considered here. This can be done, e.g., by including nontrivial wave-function renormalizations in the gradient expansion of the effective action. It has been shown in [55] that this reduces the difference between curvature and pole masses, especially for the light mesons. Phenomenologically viable spectral functions also require the inclusion of the feedback of the vector mesons themselves as well as baryonic degrees of freedom, both of which have been neglected here. In particular, the fact that our approach also allows for the computation of spectral functions at arbitrarily large chemical potential calls for an extension to include the dynamics of baryons and nuclear-matter effects in a chiral effective theory that is capable of describing both the liquid-gas transition of nuclear matter and the chiral transition in a unified framework [56]. Several of these issues have been addressed already within the FRG, showing that this method is flexible enough to tackle these ambitious tasks in the future.

ACKNOWLEDGMENTS

This work was supported by the German Federal Ministry of Education and Research (BMBF), Grant No. 05P16RDFC1. F. R. was supported by the FWF Grant No. P24780-N27 and by the DFG Collaborative Research Centre "SFB 1225 (ISOQUANT)."

APPENDIX A: DERIVATION OF FLOW EQUATIONS

In the following we provide further details on our theoretical setup as well as explicit expressions for the flow equations (see also [27,28]). The effective potential only contains the scalar meson, as well as quark-antiquark fluctuations, and is hence given by solving the flow equation obtained by applying the Wetterich equation, Eq. (12), to the ansatz for the effective action of the quark-meson model as done in [27,28,30], which yields

$$\partial_k U_k = \frac{k^4}{12\pi^2}\left[\frac{1}{E_{k,\sigma}}\coth\left(\frac{E_{k,\sigma}}{2T}\right)+\frac{3}{E_{k,\pi}}\coth\left(\frac{E_{k,\pi}}{2T}\right) - \frac{2N_f N_c}{E_{k,\psi}}\left(\tanh\left(\frac{E_{k,\psi}-\mu}{2T}\right) + \tanh\left(\frac{E_{k,\psi}+\mu}{2T}\right)\right)\right]. \tag{A1}$$

The effective quasiparticle energies are given by

$$E_{k,\alpha} \equiv \sqrt{k^2 + m_{k,\alpha}^2}, \qquad \alpha \in \{\pi, \sigma, \rho, a_1, \psi\}, \tag{A2}$$

with effective masses of the quarks and mesons,

$$m_{k,\pi}^2 = 2U_k', \tag{A3}$$

$$m_{k,\sigma}^2 = 2U_k' + 4U_k''\phi_0^2, \tag{A4}$$

$$m_{k,\rho}^2 = m_{k,V}^2, \tag{A5}$$

$$m_{k,a_1}^2 = m_{k,V}^2 + g^2\phi_0^2, \tag{A6}$$

$$m_{k,\psi}^2 = h_S^2\phi_0^2, \tag{A7}$$

where primes denote derivatives with respect to the chiral invariant $\phi^2 \equiv \sigma^2 + \vec{\pi}^2$ and $\phi_0^2 = \sigma_0^2$ is meant to be the global minimum.

Flow equations for two-point functions of vector mesons transversal and longitudinal to the heat bath are defined as

$$\partial_k \Gamma_{k,\rho/a_1}^{(2),\perp}(p) = \frac{1}{2(N_f^2-1)}\mathrm{Tr}[\Pi_{\mu\nu}^{T,\perp}(p)\partial_k(\Gamma_{k,\rho/a_1}^{(2)}(p))_{\nu\sigma}^{fg}],$$
$$\partial_k \Gamma_{k,\rho/a_1}^{(2),\parallel}(p) = \frac{1}{(N_f^2-1)}\mathrm{Tr}[\Pi_{\mu\nu}^{T,\parallel}(p)\partial_k(\Gamma_{k,\rho/a_1}^{(2)}(p))_{\nu\sigma}^{fg}], \tag{A8}$$

where $f, g \in \{1, .., (N_f^2-1)\}$ are adjoint flavor indices. The three dimensionally transverse and four dimensionally longitudinal projection operators are defined by

$$\Pi_{\mu\nu}^{T,\perp}(p) = \begin{cases} 0 & \text{if } \mu = 0 \text{ or } \nu = 0 \\ \delta_{\mu\nu} - \frac{p_\mu p_\nu}{\vec{p}^2} & \text{else,} \end{cases}$$
$$\Pi_{\mu\nu}^{T,\parallel}(p) = \delta_{\mu\nu} - \frac{p_\mu p_\nu}{p^2} - \Pi_{\mu\nu}^{T}(p), \tag{A9}$$

with

$$\Pi^{T}_{\mu\nu}(p) = \Pi^{T,\perp}_{\mu\nu}(p) + \Pi^{T,\parallel}_{\mu\nu}(p) = \delta_{\mu\nu} - \frac{p_\mu p_\nu}{p^2}. \quad \text{(A10)}$$

For vanishing external spatial momentum, $\vec{p} = 0$, we find that longitudinal and transverse parts of the flow equations coincide,

$$\partial_k \Gamma^{(2),\perp}_{k,\rho/a_1}(p_0) = \partial_k \Gamma^{(2),\parallel}_{k,\rho/a_1}(p_0). \quad \text{(A11)}$$

As illustrated diagrammatically in Fig. 2, the flow equations for the ρ and a_1 two-point functions read more explicitly,

$$\partial_k \Gamma^{(2),\perp}_{k,\rho}(p_0) = J^{\pi\pi}_{k,\rho}(p_0) - \frac{1}{2} I^{\pi}_{k,\rho} - 2J^{\psi\bar{\psi}}_{k,\rho}(p_0), \quad \text{(A12)}$$

$$\partial_k \Gamma^{(2),\perp}_{k,a_1}(p_0) = J^{\sigma\pi}_{k,a_1}(p_0) + J^{\pi\sigma}_{k,a_1}(p_0) - \frac{1}{2} I^{\pi}_{k,a_1} - \frac{1}{2} I^{\sigma}_{k,a_1} - 2J^{\psi\bar{\psi}}_{k,a_1}(p_0). \quad \text{(A13)}$$

The loop functions are defined as

$$I^{\beta}_{k,\alpha} \equiv \mathrm{Tr}[\partial R^{\beta}_k(q) G_{k,\beta}(q) \Gamma^{(4)}_{k,\beta\alpha} G_{k,\beta}(q)], \quad \text{(A14)}$$

$$J^{\beta\gamma}_{k,\alpha}(p) \equiv \mathrm{Tr}[\partial R^{\beta}_k(q+p) G_{k,\beta}(q+p) \Gamma^{(3)}_{k,\beta\gamma\alpha} \times G_{k,\gamma}(q) \Gamma^{(3)}_{k,\gamma\beta\alpha} G_{k,\beta}(q+p)], \quad \text{(A15)}$$

with a scale-dependent regulated propagator

$$G_{k,\alpha}(q) \equiv (\Gamma^{(2)}_{k,\alpha} + R^{\beta}_k(q))^{-1}. \quad \text{(A16)}$$

The trace includes summations over all internal indices as well as a loop momentum integration which, for finite temperature, turns into a spatial integration and a summation over Matsubara modes.

The regulator function has to be chosen appropriately for the different types of fields [57]. In this work we use the following three-dimensional regulator functions:

$$R^{\sigma/\pi}_k(q) = (k^2 - \vec{q}^2)\theta(k^2 - \vec{q}^2), \quad \text{(A17)}$$

$$R^{\rho/a_1}_k(q) = \Pi^{T}_{\mu\nu}(q)(k^2 - \vec{q}^2)\theta(k^2 - \vec{q}^2), \quad \text{(A18)}$$

$$R^{\psi}_k(q) = \mathrm{i}\vec{q}\left(\sqrt{k^2/\vec{q}^2} - 1\right)\theta(k^2 - \vec{q}^2). \quad \text{(A19)}$$

Explicit expressions for the three- and four-point vertices, $\Gamma^{(3)}_k$ and $\Gamma^{(4)}_k$, are given by

$$\Gamma^{(3)}_{k,\bar{\psi}\psi\rho^{\mu}_i} = \mathrm{i}h_V \gamma^{\mu} \tau_i, \quad \text{(A20)}$$

$$\Gamma^{(3)}_{k,\bar{\psi}\psi a^{\mu}_{1,i}} = \mathrm{i}h_V \gamma^{\mu}\gamma^5 \tau_i, \quad \text{(A21)}$$

$$\Gamma^{(3)}_{k,\pi_k \pi_j \rho^{\mu}_i} = \mathrm{i}g\epsilon_{ijk}(q^{\mu}_{\pi_k} - q^{\mu}_{\pi_j})\left(1 - \frac{g^2\sigma_0^2}{m^2_{k,a_1}}\right), \quad \text{(A22)}$$

$$\Gamma^{(3)}_{k,\sigma\pi_j a^{\mu}_{1,i}} = \mathrm{i}g\delta_{jl}(q^{\mu}_{\sigma} - q^{\mu}_{\pi_j}), \quad \text{(A23)}$$

$$\Gamma^{(4)}_{k,\pi_l \pi_k \rho^{\nu}_j \rho^{\mu}_i} = g^2 \delta^{\mu\nu}(2\delta_{ij}\delta_{kl} - \delta_{ik}\delta_{jl} - \delta_{il}\delta_{jk}), \quad \text{(A24)}$$

$$\Gamma^{(4)}_{k,\sigma\sigma a^{\nu}_{1,j} a^{\mu}_{1,i}} = 2g^2 \delta_{ij}\delta^{\mu\nu}, \quad \text{(A25)}$$

$$\Gamma^{(4)}_{k,\pi_l \pi_k a^{\nu}_{1,j} a^{\mu}_{1,i}} = g^2 \delta^{\mu\nu}(\delta_{ik}\delta_{jl} + \delta_{il}\delta_{jk}). \quad \text{(A26)}$$

The flow of the scale-dependent coupling $m^2_{k,V}$ is defined by projecting on the ρ mass in the following way:

$$\partial_k m^2_{k,V} = \frac{1}{2(N_f^2 - 1)} \lim_{p\to 0} \mathrm{Tr}\left(\Pi^{T,\perp}_{\mu\nu} \frac{\delta^2 \partial_k \Gamma_k}{\delta\rho^{\mu}_i \delta\rho^{\nu}_j}\right)\Big|_{\phi=\phi_0} = \partial_k m^2_{k,\rho}. \quad \text{(A27)}$$

We note that in our approach the Euclidean curvature mass of the ρ meson is given by the vector-meson coupling $m_{k,V}$; thus, their flow equations coincide.

APPENDIX B: ANALYTIC CONTINUATION AND SPECTRAL FUNCTIONS

In order to obtain flow equations for real-time (retarded) two-point functions, an analytic continuation from imaginary to real energies has to be performed. We use the following two-step analytic continuation procedure which was developed in [27,28] for the FRG. In a first step the periodicity of the bosonic and fermionic occupation numbers, which result from the Matsubara summation over the loop energy, w.r.t. the discrete external Euclidean energy p_0, is exploited, i.e.,

$$n_{B,F}(E + \mathrm{i}p_0) \to n_{B,F}(E). \quad \text{(B1)}$$

In a second step the Euclidean energy p_0 is replaced by a continuous real frequency ω in the following way,

$$\Gamma^{(2),R}(\omega, \vec{p}) = -\lim_{\epsilon\to 0} \Gamma^{(2),E}(p_0 = -\mathrm{i}(\omega + \mathrm{i}\epsilon), \vec{p}), \quad \text{(B2)}$$

where the limit $\epsilon \to 0$ can be taken exactly for the imaginary part of the two-point functions (see Appendix C), while for the real part we use a small value of $\epsilon = 0.1$ MeV or $\epsilon = 1$ MeV in our numerical implementation.

The flow equations for the retarded two-point functions are then solved using the grid method with the initial values given by

$$\Gamma^{(2),R}_{\Lambda,\rho}(\omega, \vec{p}) = (\omega + \mathrm{i}\epsilon)^2 - \vec{p}^2 - m^2_{\Lambda,\rho}, \quad \text{(B3)}$$

$$\Gamma^{(2),R}_{\Lambda,a_1}(\omega,\vec{p}) = (\omega+\mathrm{i}\epsilon)^2 - \vec{p}^{\,2} - m^2_{\Lambda,a_1}. \tag{B4}$$

The spectral functions are essentially given by the imaginary part of the retarded propagator,

$$\rho(\omega,\vec{p}) = -\frac{1}{\pi}\mathrm{Im}G^R(\omega,\vec{p}), \tag{B5}$$

which can be expressed in terms of the retarded two-point function as

$$\rho(\omega,\vec{p}) = \frac{1}{\pi}\frac{\mathrm{Im}\Gamma^{(2),R}(\omega,\vec{p})}{(\mathrm{Re}\Gamma^{(2),R}(\omega,\vec{p}))^2 + (\mathrm{Im}\Gamma^{(2),R}(\omega,\vec{p}))^2}. \tag{B6}$$

APPENDIX C: ANALYTIC IMAGINARY PARTS

The limit $\epsilon \to 0$ in the definition of the retarded two-point functions, Eq. (B2), can be performed analytically for the imaginary part of the two-point functions in the following way. For simplicity, we discuss here the case of vanishing external spatial momentum. First we note that the imaginary parts of the retarded two-point functions are obtained from those of the prefactors of the loop functions in Appendix F with Dirac-Sokhotsky identities,

$$\lim_{\epsilon\to 0}\mathrm{Im}\left(\frac{1}{\omega+\mathrm{i}\epsilon - E_\alpha \pm E_\beta}\right) \to -\pi\delta(\omega - E_\alpha \pm E_\beta),$$
$$\lim_{\epsilon\to 0}\mathrm{Im}\left(\frac{1}{(\omega+\mathrm{i}\epsilon - E_\alpha \pm E_\beta)^2}\right) \to \pi\delta'(\omega - E_\alpha \pm E_\beta).$$

Expressing these delta functions in terms of k, the flow equations for the imaginary parts of the retarded two-point functions then collapse to the $k = k_0$ values which solve

$$\omega - E_{k,\alpha} \pm E_{k,\beta} = 0, \tag{C1}$$

so the integrated flow equations reduce to the following form,

$$\begin{aligned}\int_{k_{\mathrm{UV}}}^{k_{\mathrm{IR}}} dk\partial_k \mathrm{Im}\Gamma^{(2)}_k &= \int_{k_{\mathrm{UV}}}^{k_{\mathrm{IR}}} dk(f(k)\delta(k-k_0) \\ &\quad + g(k)\delta'(k-k_0)) \\ &= -f(k_0) + g'(k_0),\end{aligned} \tag{C2}$$

where the generic functions $f(k)$ and $g(k)$ contain the derivatives $E'_{k,\alpha} \pm E'_{k,\beta}$ of the quasiparticle energies w.r.t. the momentum scale k in the denominator which gives rise to the van Hove singularities at saddle points.

An analogous procedure is possible at finite external spatial momentum.

APPENDIX D: REAL AND IMAGINARY PARTS OF RETARDED TWO-POINT FUNCTIONS

As described above, the real and imaginary parts of the flow equations for the vector-meson retarded two-point functions are solved separately. In the following we present results for these parts and their compositions. The zero crossings of the real parts are used here to define the mass of the particle. It agrees with the physical pole mass of a stable particle, if the imaginary part is zero at this energy as well. Otherwise it locates, at least approximately, the peak of a resonance whose width is determined by the imaginary part of the corresponding zero of the retarded two-point function on the unphysical Riemann sheet.

In Fig. 10 the real (left) and imaginary parts (right) of the vacuum ρ and a_1 retarded two-point functions are shown. The real part of the ρ retarded two-point function shows a zero crossing at $\omega = 789.3$ MeV. The related imaginary

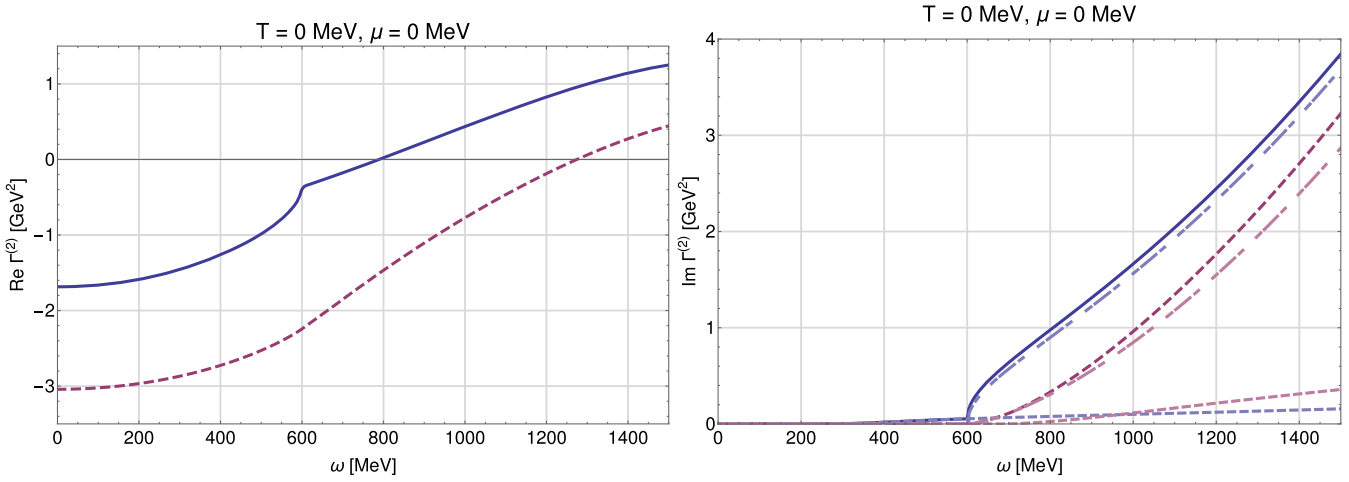

FIG. 10. Real (left) and imaginary (right) parts of the retarded two-point function of the ρ (blue) and a_1 (dashed red) meson vs external energy ω at $T = 0$ MeV and $\mu = 0$ MeV. The different contributions to the imaginary parts are shown by light dashed lines (right): $\rho^*/a_1^* \to \psi + \bar{\psi}$ (upper dashed lines) and $\rho^* \to \pi + \pi$ for the ρ meson and $a_1^* \to \pi + \sigma$ for the a_1 meson (lower dashed lines).

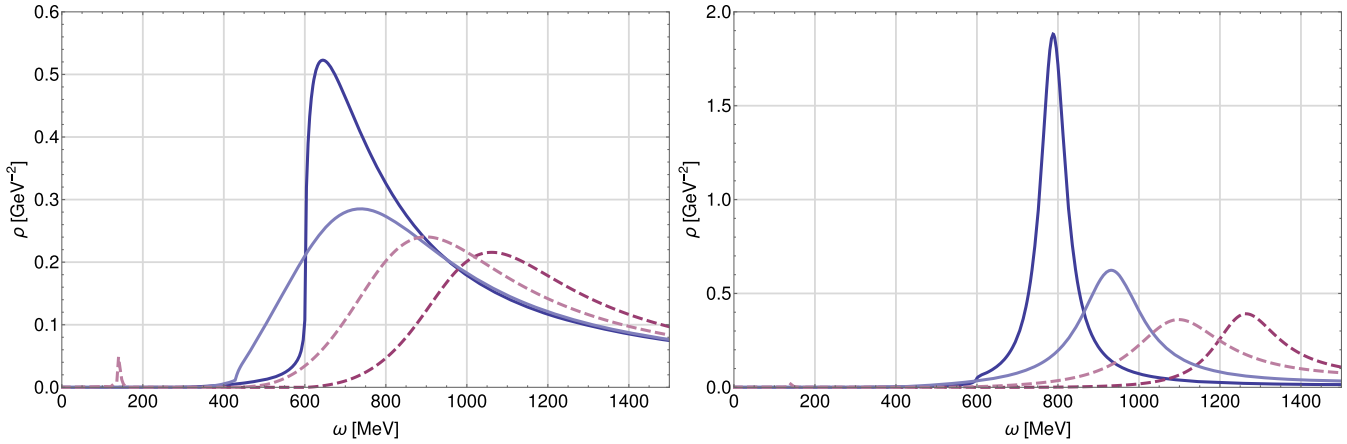

FIG. 11. Spectral functions of the ρ (blue) and a_1 (dashed red) meson at $T = 0$ MeV (normal color) and $T = 150$ MeV (light color), both for vanishing chemical potential in linear scales with (left) and without (right) a quark-antiquark decay channel.

part begins to increase significantly when the quark-antiquark decay becomes possible at around $\omega \approx 600$ MeV; the ρ peak is hence strongly suppressed. For the a_1 meson, this suppression is even stronger since the real part has a zero crossing at $\omega = 1274.7$ MeV where the imaginary part already assumes large values.

In order to see how strong the particular processes contribute to the imaginary part, these contributions are plotted separately on the right in Fig. 10. We see that for the ρ as well as for the a_1 imaginary part, the quark-antiquark decay process dominates clearly over the mesonic decay processes, even in the vacuum, where physically this decay should not be possible. However, in our approach this process is naturally present since we have no mechanism which describes confinement, and it therefore needs further investigations about how it can be suppressed or even removed in a physically reasonable way of modeling confinement.

To isolate the effects of the quark-antiquark decay channel in the spectral functions, Fig. 11 shows the full ρ and a_1 spectral functions (left) in comparison with spectral functions where the quark-antiquark contributions have been removed by hand from the imaginary parts of the two-point functions (right) in the vacuum and at $T = 150$ MeV for vanishing chemical potential, here both plotted on a linear scale. The increasing temperature leads to a melting, especially of the ρ meson spectral function, and a shift of the pole mass peaks towards each other in both cases. Additionally, due to the thermal capture process, in the a_1 spectral function a small peak arises for lower energies. Without the quark-antiquark decay channel, the peaks are less suppressed and concentrated around the masses defined by the zero crossing of the real part. As shown in Fig. 10 on the right, the quarks above threshold give by far dominant contributions to the imaginary parts and therefore shift the positions of the mass peaks in the spectral functions as well, which can be seen by comparing both sides in Fig. 11. For a better comparison with Fig. 8 in the main text, the vacuum spectral functions without the quark-antiquark decay channel are also plotted on logarithmic scales in Fig. 12. Here we see broad peaks concentrated around the pole masses of the ρ and a_1 mesons.

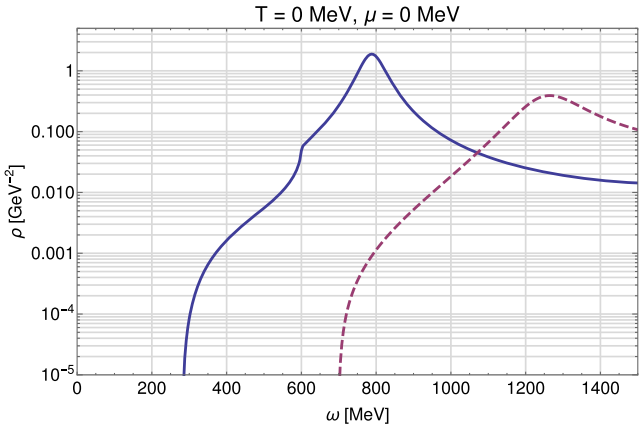

FIG. 12. Vacuum spectral functions of the ρ (blue) and a_1 (dashed red) meson without a quark-antiquark decay channel.

APPENDIX E: AVAILABLE PROCESSES

In this section we summarize and discuss the different scattering and absorption or emission processes that can occur within our framework. We divide these processes into timelike and spacelike types. Timelike processes involve off-shell particles with a total energy ω that is larger than their spatial momentum $|\vec{p}|$, i.e., $\omega \geq |\vec{p}|$, while spacelike processes involve a particle excitation with $\omega < |\vec{p}|$ (see Fig. 13).

The available timelike processes for an external off-shell ρ meson, denoted as ρ^*, are given by

$$\rho^* \to \pi + \pi, \qquad \omega \geq \sqrt{(2m_\pi)^2 + \vec{p}^2}, \tag{E1}$$

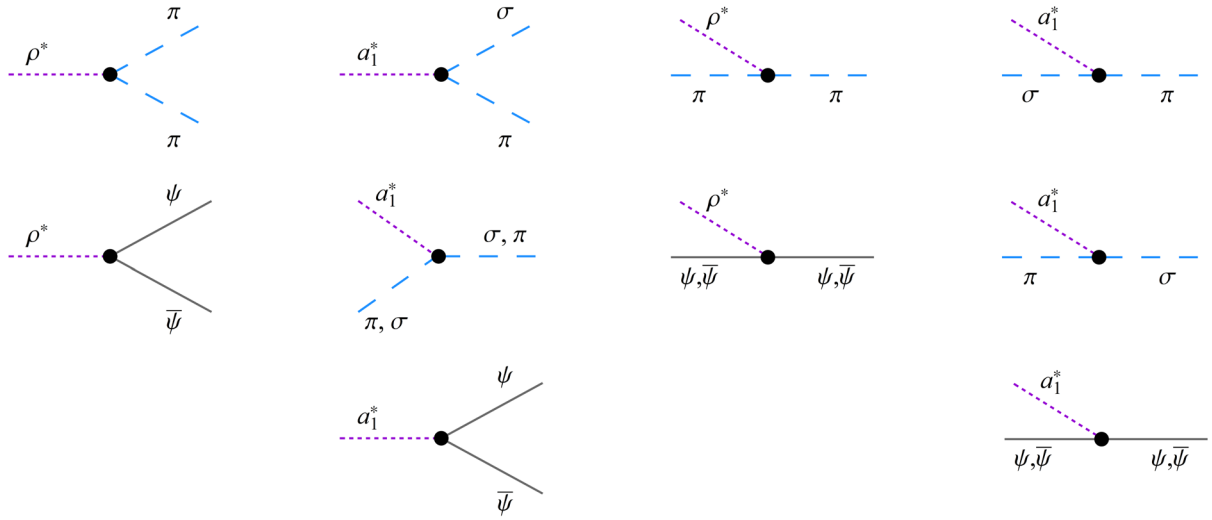

FIG. 13. Collection of the possible timelike, $p^2 = \omega^2 - \vec{p}^2 > 0$, and spacelike, $p^2 < 0$, processes. Asterisks denote off-shell particles with total energy ω and spatial momentum $\vec{p}$, while others represent on-shell particles from the heat bath. First column: Timelike decay channels for the ρ meson. Second column: Timelike decay channels for the a_1 meson. Third column: Absorption of a spacelike ρ excitation. Fourth column: Absorption of a spacelike a_1 excitation. In addition, particle-hole excitations on the Fermi surface of (anti) quarks are possible (see text for details).

$$\rho^* \to \bar{\psi} + \psi, \qquad \omega \geq \sqrt{(2m_\psi)^2 + \vec{p}^2}, \tag{E2}$$

where the kinematic constraints follow from energy conservation. We note that particles without asterisks represent on-shell particles and that their masses are given by the Euclidean masses in our truncation. Moreover, if there are particles available from the heat bath, the inverse of the above processes is also possible, giving rise to an equilibrium between direct and inverse processes. The corresponding statistical weight factors can be easily read off from the corresponding loop functions (see the discussion in Appendix F).

The timelike processes for an a_1^* meson are given by

$$a_1^* \to \sigma + \pi, \quad \omega \geq \sqrt{(m_\sigma + m_\pi)^2 + \vec{p}^2}, \tag{E3}$$

$$a_1^* + \pi \to \sigma, \quad |\vec{p}| \leq \omega \leq (m_\sigma - m_\pi)\sqrt{1 + \frac{\vec{p}^2}{\Delta m^2}}, \tag{E4}$$

$$a_1^* + \sigma \to \pi, \quad |\vec{p}| \leq \omega \leq (m_\pi - m_\sigma)\sqrt{1 + \frac{\vec{p}^2}{\Delta m^2}}, \tag{E5}$$

$$a_1^* \to \bar{\psi} + \psi, \quad \omega \geq \sqrt{(2m_\psi)^2 + \vec{p}^2}, \tag{E6}$$

with $\Delta m^2 \equiv (m_\sigma - m_\pi)^2$. The first and last processes describe standard decay channels, while (E4) and (E5) describe capture processes which are only possible if there are particles from the heat bath available and if the kinematic constraints are fulfilled. In general, only the capture process $a_1^* + \pi \to \sigma$ is possible since the pion mass is usually smaller than the sigma mass.

We now turn to the spacelike processes which, in the case of the ρ meson, are given by

$$\left.\begin{aligned} \rho^* + \pi &\to \pi \\ \rho^* + \psi &\to \psi \end{aligned}\right\} 0 \leq \omega \leq |\vec{p}| \tag{E7}$$

where ψ represents both quarks and antiquarks. These processes describe the absorption or, when considering the inverse processes, the emission of a spacelike ρ meson.

Similarly, the spacelike processes for the a_1 meson are given by

$$\left.\begin{aligned} a_1^* + \sigma &\to \pi \\ a_1^* + \pi &\to \sigma \\ a_1^* + \psi &\to \psi \end{aligned}\right\} 0 \leq \omega \leq |\vec{p}|, \tag{E8}$$

with ψ again representing both quarks and antiquarks. We note that all spacelike processes are only possible if there are particles from the heat bath available.

In addition to the processes discussed so far, particle-hole excitations of quarks or antiquarks are also possible at finite chemical potential as soon as a Fermi sphere starts building up. These processes can be induced by an external ρ or a_1 meson with an energy-momentum configuration that allows for an excitation of particle-hole pairs in the vicinity of the Fermi surface (see also Appendix F). These particle-hole processes lead to interesting phenomena such as long-wavelength collective excitations such as sound waves, which will be discussed in future applications of our approach.

APPENDIX F: EXPLICIT EXPRESSIONS FOR THE LOOP FUNCTIONS

In this section we provide explicit expressions for the loop functions appearing in the flow equations for the retarded two-point functions (cf. Appendix A).

The loop functions are written in a form that allows for an easy interpretation in terms of physical processes. We divide these processes into three categories: vacuum processes, capture processes, and particle-hole processes. Processes that can occur in the vacuum are associated with statistical weight factors of the form

$$(1+n_B(E_\alpha))(1+n_B(E_\beta))-n_B(E_\alpha)n_B(E_\beta),$$

which relates to the process $\omega \to E_\alpha + E_\beta$ and its inverse process $E_\alpha + E_\beta \to \omega$. Capture processes are only possible when there are particles from a heat bath available. They carry weight factors like

$$n_B(E_\alpha)(1+n_B(E_\beta))-n_B(E_\beta)(1+n_B(E_\alpha))$$

and correspond to processes like $\omega + E_\alpha \to E_\beta$ and its inverse. Particle-hole processes are proportional to the derivative of the occupation number, e.g., $n_B'(E_\alpha)$.

The momentum-independent loop functions $I_{k,\rho/a_1}$ only contribute to the real part of the retarded two-point functions. They are given by

$$I^{\pi}_{k,\rho} = \frac{k^4 g^2}{3E^3_{k,\pi}\pi^2}[1+2n_B(E_{k,\pi})-2E_{k,\pi}n_B'(E_{k,\pi})],$$

$$I^{\alpha}_{k,a_1} = \frac{k^4 g^2}{6E^3_{k,\alpha}\pi^2}[1+2n_B(E_{k,\alpha})-2E_{k,\alpha}n_B'(E_{k,\alpha})],$$

with $\alpha \in \{\pi,\sigma\}$.

The momentum-dependent loop functions $J_{k,\rho/a_1}(\omega)$ contribute to both the real and imaginary parts and therefore encode information about possible decay processes. Split into contributions related to the different processes, they are listed in Eqs. (F4)–(F6). For the sake of simplicity we drop the external spatial momentum dependence here. In this case the theta function in the regulator functions, Eqs. (A17)–(A19), has to be evaluated numerically. For the external energy ω we use the notation $\omega_+ \to \omega + i\epsilon$.

The loop function $J^{\pi\pi}_{k,\rho}(\omega)$, Eq. (F4), describes the decay of an off-shell ρ meson into a pion pair, $\rho^* \to \pi+\pi$, and its inverse process $\pi+\pi \to \rho^*$. The imaginary part of these processes is nonvanishing when it becomes energetically possible, e.g., $\omega \geq 2E_{k,\pi}$ for the former process. The mesonic decay channel for the a_1 meson is described by the loop function $J^{\alpha\beta}_{k,a_1}(\omega)$, Eq. (F5), with $\alpha,\beta \in \{\pi,\sigma\}$, but distinguished. Here we also have the vacuum processes $a_1^* \to \alpha+\beta$ and $\alpha+\beta \to a_1^*$ but also capture processes as described above. These processes are of the form $a_1^* + \alpha/\beta \to \beta/\alpha$ and are described by single occupation numbers $\pm n_B(E_{k,\alpha/\beta})$. For $T \to 0$ these contributions vanish completely, in contrast to the vacuum processes. The mesonic decay in a quark-antiquark pair is described by the loop function $J^{\psi\bar{\psi}}_{k,\alpha}(\omega)$, Eq. (F6). Here we also have the vacuum process $\rho^*/a_1^* \to \psi+\bar{\psi}$ and its inverse $\psi+\bar{\psi} \to \rho^*/a_1^*$. The form $(1-n_F(E_{k,\psi}))$ reflects Pauli blocking: Available states for the decay products are suppressed since there are real fermions in the heat bath. The coefficients $\tilde{E}^{(\alpha)}_{1,k}, \tilde{E}^{(\alpha)}_{2,k}$ and $\tilde{E}^{(\alpha)}_{3,k}$ are defined by

$$\tilde{E}^{(\alpha)}_{1,k} = 8k^2 + L^{(\alpha)}_k, \tag{F1}$$

$$\tilde{E}^{(\alpha)}_{2,k} = 8m^2_{k,\psi} - L^{(\alpha)}_k, \tag{F2}$$

$$\tilde{E}^{(\alpha)}_{3,k} = -4E^2_{k,\psi} - 8m^2_{k,\psi} + L^{(\alpha)}_k, \tag{F3}$$

with $L^{(\rho)}_k = 12m^2_{k,\psi}$ and $L^{(a_1)}_k = 0$.

Additionally, there are terms proportional to a derivative of an occupation number which are connected to particle-hole processes.

$$\begin{aligned} J^{\pi\pi}_{k,\rho}(\omega,|\vec{p}|=0) = &-\frac{1}{(\omega_+ - 2E_{k,\pi})}\frac{k^6 g^2 m^4_{k,\rho}}{15\pi^2 E^3_{k,\pi} m^4_{k,a_1}}[1+2n_B(E_{k,\pi})-E_{k,\pi}n_B'(E_{k,\pi})] \\ &+\frac{1}{(\omega_+ - 2E_{k,\pi})^2}\frac{k^6 g^2 m^4_{k,\rho}}{15\pi^2 E^3_{k,\pi} m^4_{k,a_1}}[1+2n_B(E_{k,\pi})] \\ &+\frac{1}{(\omega_+ + 2E_{k,\pi})}\frac{k^6 g^2 m^4_{k,\rho}}{15\pi^2 E^3_{k,\pi} m^4_{k,a_1}}[1+2n_B(E_{k,\pi})-E_{k,\pi}n_B'(E_{k,\pi})] \\ &+\frac{1}{(\omega_+ + 2E_{k,\pi})^2}\frac{k^6 g^2 m^4_{k,\rho}}{15\pi^2 E^3_{k,\pi} m^4_{k,a_1}}[1+2n_B(E_{k,\pi})], \end{aligned} \tag{F4}$$

$$
\begin{aligned}
J^{\alpha\beta}_{k,a_1}(\omega,|\vec{p}|=0) = &+\frac{1}{(\omega_+ + E_{k,\alpha}+E_{k,\beta})}\frac{k^6g^2}{30\pi^2E^3_{k,\alpha}E_{k,\beta}}[1+n_B(E_{k,\alpha})+n_B(E_{k,\beta})-E_{k,\alpha}n'_B(E_{k,\alpha})]\\
&+\frac{1}{(\omega_+ + E_{k,\alpha}+E_{k,\beta})^2}\frac{k^6g^2}{30\pi^2E^2_{k,\alpha}E_{k,\beta}}[1+n_B(E_{k,\alpha})+n_B(E_{k,\beta})]\\
&-\frac{1}{(\omega_+ - E_{k,\alpha}-E_{k,\beta})}\frac{k^6g^2}{30\pi^2E^3_{k,\alpha}E_{k,\beta}}[1+n_B(E_{k,\alpha})+n_B(E_{k,\beta})-E_{k,\alpha}n'_B(E_{k,\alpha})]\\
&+\frac{1}{(\omega_+ - E_{k,\alpha}-E_{k,\beta})^2}\frac{k^6g^2}{30\pi^2E^2_{k,\alpha}E_{k,\beta}}[1+n_B(E_{k,\alpha})+n_B(E_{k,\beta})]\\
&+\frac{1}{(\omega_+ - E_{k,\alpha}+E_{k,\beta})}\frac{k^6g^2}{30\pi^2E^3_{k,\alpha}E_{k,\beta}}[n_B(E_{k,\alpha})-n_B(E_{k,\beta})-E_{k,\alpha}n'_B(E_{k,\alpha})]\\
&+\frac{1}{(\omega_+ - E_{k,\alpha}+E_{k,\beta})^2}\frac{k^6g^2}{30\pi^2E^2_{k,\alpha}E_{k,\beta}}[-n_B(E_{k,\alpha})+n_B(E_{k,\beta})]\\
&+\frac{1}{(\omega_+ + E_{k,\alpha}-E_{k,\beta})}\frac{k^6g^2}{30\pi^2E^3_{k,\alpha}E_{k,\beta}}[-n_B(E_{k,\alpha})+n_B(E_{k,\beta})+E_{k,\alpha}n'_B(E_{k,\alpha})]\\
&+\frac{1}{(\omega_+ + E_{k,\alpha}-E_{k,\beta})^2}\frac{k^6g^2}{30\pi^2E^2_{k,\alpha}E_{k,\beta}}[-n_B(E_{k,\alpha})+n_B(E_{k,\beta})],
\end{aligned}
\tag{F5}
$$

$$
\begin{aligned}
J^{\psi\bar{\psi}}_{k,\alpha}(\omega,|\vec{p}|=0) = &-\frac{1}{(\omega_+)}\frac{k^4h_V^2}{6\pi^2E^3_{k,\psi}}[\tilde{E}^{(\alpha)}_{3,k}(n'_F(E_{k,\psi}+\mu)-n'_F(E_{k,\psi}-\mu))]\\
&-\frac{1}{(\omega_+ - 2E_{k,\psi})}\frac{k^4h_V^2}{6\pi^2E^4_{k,\psi}}[\tilde{E}^{(\alpha)}_{2,k}(1-n_F(E_{k,\psi}-\mu)-n_F(E_{k,\psi}+\mu))-E_{k,\psi}\tilde{E}^{(\alpha)}_{1,k}n'_F(E_{k,\psi}+\mu)]\\
&-\frac{1}{(\omega_+ - 2E_{k,\psi})^2}\frac{k^4h_V^2}{6\pi^2E^3_{k,\psi}}[\tilde{E}^{(\alpha)}_{1,k}(1-n_F(E_{k,\psi}-\mu)-n_F(E_{k,\psi}+\mu))]\\
&+\frac{1}{(\omega_+ + 2E_{k,\psi})}\frac{k^4h_V^2}{6\pi^2E^4_{k,\psi}}[\tilde{E}^{(\alpha)}_{2,k}(1-n_F(E_{k,\psi}-\mu)-n_F(E_{k,\psi}+\mu))-E_{k,\psi}\tilde{E}^{(\alpha)}_{1,k}n'_F(E_{k,\psi}-\mu)]\\
&-\frac{1}{(\omega_+ + 2E_{k,\psi})^2}\frac{k^4h_V^2}{6\pi^2E^3_{k,\psi}}[\tilde{E}^{(\alpha)}_{1,k}(1-n_F(E_{k,\psi}-\mu)-n_F(E_{k,\psi}+\mu))].
\end{aligned}
\tag{F6}
$$

[1] M. A. Stephanov, Prog. Theor. Phys. Suppl. **153**, 139 (2004); Int. J. Mod. Phys. A **20**, 4387 (2005).
[2] P. Braun-Munzinger and J. Wambach, Rev. Mod. Phys. **81**, 1031 (2009).
[3] R. Rapp, Adv. High Energy Phys. **2013**, 148253 (2013).
[4] H. van Hees and R. Rapp, Nucl. Phys. **A827**, 341C (2009); **A827**, 495 (2009).
[5] R. Rapp, *Proc. Sci.*, CPOD2013 (2013) 008 [arXiv: 1306.6394].
[6] R. Rapp and J. Wambach, arXiv:nucl-th/0001014.
[7] G. Brown and M. Rho, Phys. Rev. Lett. **66**, 2720 (1991).
[8] P. M. Hohler and R. Rapp, Phys. Lett. B **731**, 103 (2014).
[9] R. Rapp, G. Chanfray, and J. Wambach, Nucl. Phys. **A617**, 472 (1997).
[10] R. D. Pisarski, Phys. Lett. **110B**, 155 (1982).
[11] R. Rapp, J. Wambach, and H. van Hees, Landolt-Bornstein **23**, 134 (2010).
[12] J. J. Sakurai, Ann. Phys. (N.Y.) **11**, 1 (1960).
[13] D. Schildknecht, Acta Phys. Pol. B **37**, 595 (2006).
[14] B. W. Lee and H. T. Nieh, Phys. Rev. **166**, 1507 (1968).
[15] M. Urban, M. Buballa, and J. Wambach, Nucl. Phys. **A697**, 338 (2002).
[16] F. Rennecke, Phys. Rev. D **92**, 076012 (2015).
[17] J. Eser, M. Grahl, and D. H. Rischke, Phys. Rev. D **92**, 096008 (2015).
[18] J. Polonyi, Central Eur. J. Phys. **1**, 1 (2003).
[19] C. Bagnuls and C. Bervillier, Phys. Rep. **348**, 91 (2001).
[20] H. Gies, arXiv:hep-ph/0611146.
[21] J. Berges, N. Tetradis, and C. Wetterich, Phys. Rep. **363**, 223 (2002).

[22] J. M. Pawlowski, Ann. Phys. (Amsterdam) **322**, 2831 (2007).
[23] D. F. Litim and J. M. Pawlowski, J. High Energy Phys. 11 (2006) 026.
[24] L. von Smekal, Nucl. Phys. B, Proc. Suppl. **228**, 179 (2012).
[25] J. M. Pawlowski, AIP Conf. Proc. **1343**, 75 (2011).
[26] B. Delamotte, arXiv:cond-mat/0702365.
[27] R.-A. Tripolt, N. Strodthoff, L. von Smekal, and J. Wambach, Phys. Rev. D **89**, 034010 (2014).
[28] R.-A. Tripolt, L. von Smekal, and J. Wambach, Phys. Rev. D **90**, 074031 (2014).
[29] R.-A. Tripolt, L. von Smekal, and J. Wambach, arXiv:1605.00771.
[30] B.-J. Schaefer and J. Wambach, Nucl. Phys. **A757**, 479 (2005).
[31] B.-J. Schaefer and J. Wambach, Phys. Part. Nucl. **39**, 1025 (2008).
[32] B.-J. Schaefer, J. M. Pawlowski, and J. Wambach, Phys. Rev. D **76**, 074023 (2007).
[33] T. K. Herbst, J. M. Pawlowski, and B.-J. Schaefer, Phys. Lett. B **696**, 58 (2011).
[34] N. Strodthoff, B.-J. Schaefer, and L. von Smekal, Phys. Rev. D **85**, 074007 (2012).
[35] M. Mitter and B.-J. Schaefer, Phys. Rev. D **89**, 054027 (2014).
[36] J. M. Pawlowski and F. Rennecke, Phys. Rev. D **90**, 076002 (2014).
[37] N. Khan, J. M. Pawlowski, F. Rennecke, and M. M. Scherer, arXiv:1512.03673.
[38] N. P. M. Holt, P. M. Hohler, and R. Rapp, Phys. Rev. D **87**, 076010 (2013).
[39] P. M. Hohler and R. Rapp, Ann. Phys. (Amsterdam) **368**, 70 (2016).
[40] S. Floerchinger, J. High Energy Phys. 05 (2012) 021.
[41] K. Kamikado, N. Strodthoff, L. von Smekal, and J. Wambach, Eur. Phys. J. C **74**, 2806 (2014).
[42] J. M. Pawlowski and N. Strodthoff, Phys. Rev. D **92**, 094009 (2015).
[43] J. Braun, L. Fister, J. M. Pawlowski, and F. Rennecke, Phys. Rev. D **94**, 034016 (2016).
[44] M. Mitter, J. M. Pawlowski, and N. Strodthoff, Phys. Rev. D **91**, 054035 (2015).
[45] K. Fukushima, Phys. Lett. B **591**, 277 (2004).
[46] F. Marhauser and J. M. Pawlowski, arXiv:0812.1144.
[47] V. Skokov, B. Stokic, B. Friman, and K. Redlich, Phys. Rev. C **82**, 015206 (2010).
[48] C. Wetterich, Phys. Lett. B **301**, 90 (1993).
[49] R.-A. Tripolt, I. Haritan, J. Wambach, and N. Moiseyev, arXiv:1610.03252.
[50] S. Carignano, M. Buballa, and B.-J. Schaefer, Phys. Rev. D **90**, 014033 (2014).
[51] R.-A. Tripolt, B.-J. Schaefer, L. von Smekal, and J. Wambach (unpublished).
[52] T. D. Cohen, Phys. Rev. Lett. **91**, 222001 (2003).
[53] R. Rapp and J. Wambach, Adv. Nucl. Phys. **25**, 1 (2000).
[54] S.-x. Qin and D. H. Rischke, Phys. Rev. D **88**, 056007 (2013).
[55] A. J. Helmboldt, J. M. Pawlowski, and N. Strodthoff, Phys. Rev. D **91**, 054010 (2015).
[56] J. Weyrich, N. Strodthoff, and L. von Smekal, Phys. Rev. C **92**, 015214 (2015).
[57] J. M. Pawlowski, M. M. Scherer, R. Schmidt, and S. J. Wetzel, arXiv:1512.03598.